INCLUSIVE PUBLISHING
TRUSTED SCIENCE

PAPER • OPEN ACCESS

Enhanced nonlinear absorption and photoluminescence properties of Zn, Fe, Cu, V and Ni doped MoO_3 transition metal oxide thin films

To cite this article: Yasemin Pepe *et al* 2024 *Phys. Scr.* **99** 025216

View the article online for updates and enhancements.

Physica Scripta

PAPER

Enhanced nonlinear absorption and photoluminescence properties of Zn, Fe, Cu, V and Ni doped MoO$_3$ transition metal oxide thin films

Yasemin Pepe[1],[*] , Yusuf Tutel[2], Ali Deniz Ucar[2], Eda Cevik[2], Ahmet Karatay[1],
Husnu Emrah Unalan[2],[3],[*] and Ayhan Elmali[1]

[1] Department of Engineering Physics, Faculty of Engineering, Ankara University, 06100, Ankara, Turkey
[2] Department of Metallurgical and Materials Engineering, Middle East Technical University (METU), 06800 Ankara, Turkey
[3] Energy Storage Materials and Devices Research Center (ENDAM), Middle East Technical University (METU), 06800 Ankara, Turkey
[*] Authors to whom any correspondence should be addressed.

E-mail: ypepe@.ankara.edu.tr and unalan@metu.edu.tr

Abstract

In this study, the effect of the dopant element on the linear, nonlinear absorption and optical limiting properties of ultrasonically sprayed MoO$_3$ thin films is presented. The linear optical results showed an increase with the density of the defect states in the bandgap with doping, in conjunction with a decrease in bandgap energy and an increase in Urbach energy. Broad photoluminescence emissions are detected in the range of 350 and 600 nm, decreasing in intensity by doping. To reveal the defect states effects' on the nonlinear absorption (NA) behavior, OA Z-scan data were analyzed with two theoretical models considering only two photon absorption (2PA) (model 1), and one photon absorption (OPA), 2PA and free carrier absorption (model 2). The NA behavior is observed and found to get enhanced by increasing input intensity and doping atoms due to generation of new oxygen vacancies and formation of further defect states. The NA coefficient values of the thin films in model 2 are 100 times higher than that of 2PA coefficient values in model 1. This result revealed the strong effect of defect states on the NA behavior. Among the investigated dopant atoms, Cu resulted in enhanced NA due to the higher density of defect states. While the genuine 2PA is the dominant NA mechanism for V and Fe doped MoO$_3$ thin films, OPA and 2PA are the dominant NA mechanisms for the Ni, Zn and Cu doped MoO$_3$ thin films due to their higher concentration of defect states. Cu-doped MoO$_3$ thin film has a lower optical limiting threshold of 0.026 mJ/cm^2 due to its enhanced NA behavior. Considering the results obtained, this study opens the door to the potential of doped MoO$_3$ thin films to be used as optical limiters in the visible wavelength region.

1. Introduction

Transition metal oxides (TMOs) have been widely investigated owing to their optical, electrical, chemical properties and distinct morphologies. Among all TMOs, molybdenum trioxide (MoO$_3$) is highly promising for optoelectronic applications due to its wide bandgap and various oxidation states. It is an n-type semiconductor and has three polymorphic phases, which are metastable hexagonal phase (h-MoO$_3$), metastable monoclinic phase (β-MoO$_3$) and stable orthorhombic phase (α-MoO$_3$). The α-MoO$_3$ phase has a layered structure and is stacked in the [0k0] direction. Various deposition techniques are reported in the literature for the fabrication of MoO$_3$ thin films, such as the sol–gel method [1, 2], spray pyrolysis [3, 4], electrodeposition [5], ultrasonic spray deposition [6] and physical vapor deposition [7]. The ultrasonic spray deposition (USD) method, among other solution-based methods, is a convenient, easy and relatively low-cost technique for the deposition of thin films. Deposition is usually carried out in atmospheric conditions. Various metal oxide thin films are effectively deposited using USD method [8–15].

Doping introduces lattice strain and improve optical properties of MoO_3 and tune its wide optical bandgap [2, 4, 16–18]. For instance, Boukhachem *et al* prepared MoO_3:Co thin films on glass substrates through spray pyrolysis [19]. The effect of Co concentration on the optical transmittance, reflectance, Urbach energy and optical bandgap values were investigated. A direct correlation between doping concentration and magnitude of optical bandgap is observed. Sen *et al* found that the optical bandgap of hydrothermally synthesized MoO_3:Dy nanobelts varies with the amount of dopants [17]. In another study, the broadened transmittance and optical bandgap was observed for MoO_3:Ag with an increase in the dopant concentration [18].

Nonlinear absorption (NA) is a density-dependent transmittance that causes radical changes in the ground state of the material as a result of strong light–matter interaction. In a non-resonant system, two photons are simultaneously absorbed via a genuine two photon absorption (2PA), while in a resonant system the actual intermediate state is sequential two photon absorption (two-step sequential excited state absorption (ESA)). Both 2PA and ESA occur in a near-resonant system state, and the process is termed effective 2PA [20, 21]. Very recently, the effect of defect states on NA has been investigated for amorphous and polycrystalline semiconductors [22–25], as well as for polymeric nanofibers [22, 23]. Those studies showed that NA performance can be tuned by increasing the defect density [24–26, 28]. This strategy is a crucial point for applications such as optical limiters. Moreover, the distribution of defect states within the bandgap is another critical point for observing NA performance in a wide spectral range. At this point the value of the bandgap is important as well as the distribution of defect states within the bandgap.

Only Lin *et al* demonstrated ultrafast photonic applications of Sn-modified MoO_3 nanoribbons [29]. Some nonlinear optical properties such as optical damage power threshold, light absorption and saturable absorption were improved through Sn doping, but the optical limiting properties were not reported. Doping MoO_3 with Zn, Fe, Cu, V and Ni cause new defect states related to oxygen vacancies and point defects. Defects, especially those caused by oxygen vacancies have a significant effect on NA and optical limiting. Although there are some studies on the doping effect related linear optical properties of MoO_3, as far as we know, there is no study investigating both NA and optical limiting feature of MoO_3 doped with Fe, Cu, Zn, V and Ni atoms. Therefore, in this study, the doping (Fe, Cu, Zn, V, Ni) effect related structure, morphology, NA and optical limiting features of ultrasonic spray-deposited MoO_3 thin films were investigated. Using 4 ns pulsed Q switched Nd:YAG laser with an 532 nm emission wavelength, the NA and optical limiting features of the MoO_3 nanostructures were revealed by open aperture (OA) Z-scan technique. Two theoretical models were used to determine the 2PA coefficients, and NA coefficient. Femtosecond transient absorption spectroscopy measurements were also performed to identify ultrafast carrier dynamics of the thin films.

2. Experimental

2.1. Thin film deposition techniques

Microscopic glass slides were purchased from ISOLAB. Ammonium heptamolybdate tetrahydrate $((NH_4)_6Mo_7O_{24} \cdot 4H_2O)$, iron(III) nitrate nonahydrate $(Fe(NO_3)_3 \cdot 9H_2O)$, zinc nitrate hexahydrate $(Zn(NO_3)_2 \cdot 6H_2O)$, copper(II) nitrate trihydrate $(Cu(NO_3)_2 \cdot 3H_2O)$, ammonium metavanadate (NH_4VO_3), nickel(II) nitrate hexahydrate $(Ni(NO_3)_2 \cdot 6H_2O)$, ethanol and acetone were purchased from Sigma-Aldrich. Deionized water (DI) (18.3 MΩ) was used in all steps. All chemicals were used without purification. Microscopic glass slides were cut to 2 cm $\times$ 2 cm dimensions and cleaned sequentially with acetone, ethanol, and DI water for 15 min each using an ultrasonic bath. All substrates were dried under nitrogen flow. The aqueous precursor solution was obtained using $(NH_4)_6Mo_7O_{24} \cdot 4H_2O$. To fabricate 5 wt% doped MoO_3 thin films, specific amounts of different salts, which were $Fe(NO_3)_3 \cdot 9H_2O$, $Zn(NO_3)_2 \cdot 6H_2O$, $Cu(NO_3)_2 \cdot 3H_2O$, NH_4VO_3 and $Ni(NO_3)_2 \cdot 6H_2O$ were added to the precursor solution. Firstly, 5 mM $(NH_4)_6Mo_7O_{24} \cdot 4H_2O$ precursor solution was prepared in 200 ml of DI water and it was directly used for MoO_3 deposition. To prepare 5 wt% Fe, Zn, Cu, V and Ni doped MoO_3 precursor solutions, 0.244 g $Fe(NO_3)_3 \cdot 9H_2O$, 0.153 g $Zn(NO_3)_2 \cdot 6H_2O$, 0.128 g $Cu(NO_3)_2 \cdot 3H_2O$, 0.080 g NH_4VO_3 and 0.166 g $Ni(NO_3)_2 \cdot 6H_2O$ were added into 200 ml of precursor MoO_3 salt solution, respectively. All precursor solutions were stirred vigorously for 1 h at room temperature. The pH of all precursor solutions were around 5.0 (figure S1). The precursor solutions were sprayed onto glass substrates using a commercial USD system (Exacta Coat, Sono-Tek) using the ultrasonic Vortex nozzle (operated at 120 kHz), which produces stable and conical spray patterns onto pre-heated substrates (T = 150 °C). The distance between the samples and the spraying nozzle was 9.5 cm. The solution flow rate was set to 0.2 ml min^{-1} and clean air at 3 kPa was used as the carrier gas. The ultrasonic nozzle was moved with a constant speed of 40 mm s^{-1} in x-y directions following an S-shaped pattern with a spacing of 1 mm. Total deposition was finalized in 10 cycles. Following deposition, all films were annealed at 400 °C for 60 min under ambient conditions. Finally, all thin films were furnace cooled to room temperature.

2.2. Structural, morphological and optical characterization techniques

The morphology of the MoO_3 thin films were examined by scanning electron microscopy (SEM). A FEI Nova Nano FEG-SEM operated at 20 kV, equipped with an energy-dispersive x-ray (EDX) analyzer. Prior to SEM analysis, a thin Au layer was deposited onto samples. The crystal structure of the thin films was determined using a Rigaku D/Max-2000 diffractometer with Cu K radiation operating at 40 kV (at a wavelength of 0.154 nm) from 10° to 70° at a scan rate of 0.5/min. Raman spectra were recorded with a BRUKER FRA 106/S spectrometer using a 532 nm Nd:YAG laser as the excitation source. Spectroscopic ellipsometer (Woollam M2000V) at three angles of incidence (65°, 70°, 75°) was used to determine the thickness of the MoO_3 thin films. The measurements revealed that all samples were around 270 nm thick. Shimadzu UV-1800 model UV–vis spectrophotometer was used to investigate the linear absorption behaviors of the MoO_3 thin films. The photoluminescence measurements were conducted by Perkin Elmer LS55 spectrophotometer at wavelength of 320 nm at room temperature. OA Z-scan experiments were conducted with a Q-switched Nd:YAG (QuantelBirillant) laser (4 ns pulse duration, 10 Hz repetition rate) at 532 nm excitation wavelength to reveal the effective nonlinear optical feature of the MoO_3 thin films. A Ti: Sapphire laser amplifier and an optical parametric amplifier system with a 52 fs pulse duration and a 1 kHz repetition rate (Spectra physics, Spitfire Pro XP, TOPAS) were used to perform the femtosecond transient absorption spectra. The charge transfer mechanisms of the thin films were revealed by pump probe experimental setup (Spectra Physics, Helios) with a white light continuum probe and obtained data were analyzed with Surface xplorer software (Ultrafast systems). The pump wavelength was chosen as 400 nm for the thin films.

3. Results and discussions

3.1. Morphological and structural analysis

Figures 1(a),(b) are evidence of polycrystalline structure and all diffraction peaks can be indexed to the orthorhombic structure of α-MoO_3 (JCPDS card No. 05–0508). The peaks of the (020), (040), (060), (110) and (021) planes are providing strong evidence of the orthorhombic α-MoO_3 phase. Moreover, the original orthorhombic structure of α-MoO_3 is not changed since no other diffraction peaks related to Fe, Zn, Cu, V, Ni or other impurities or secondary oxide phases or intermetallics are observed. This also indicated the successful incorporation of dopant atoms into the α-MoO_3 lattice. Slight shifts are observed for the (020) peaks in the doped samples relative to the bare α-MoO_3 film, as observed in the magnified diffraction peak for the (020) plane (figure 1(b)). The shifting of the (020) plane can be attributed to the lattice strain introduced to the orthorhombic α-MoO_3 structure upon doping [30–37]. Also, the strain can cause the interplanar distance to change and hence the peak angle to decrease [30, 31].

Three strong planes where k = 2, 4, 6 are observed, called (0k0) planes, indicating the presence of a layered growth structure [38]. Among these planes, the (040) plane showed the preferential orientation for bare MoO_3 thin films. However, upon doping of bare α-MoO_3 thin films, the preferential orientation changed to (020) plane. The doping element can affect the preferential orientation of the films [39, 40]. Moreover, an inverse relation of peak angle and intensity can be seen in figure 1(a), and it is compatible with Bragg's law since $I \propto \frac{1}{\sin(2\theta)}$. As the peak angle shifts to the left, the intensity of the peak may increase, and this may be associated with increased crystallinity. The peak intensity of the (020) plane varies according to the dopant element (figure 1(b)). The MoO_3:Cu thin film has the highest intensity peak among other thin films.

Raman spectroscopy was used for the further structural characterization and quantification of defects for bare and doped MoO_3 thin films (figure 1(c),(d)). The positions of all detected Raman peaks are in good agreement with studies in the literature [41–46]. The Raman signal observed at 996 cm^{-1} corresponds to the asymmetric stretching of $Mo=O_1$ along the b-axis direction, whereas the peak at 819 cm^{-1} is attributable to the symmetric stretching of $Mo-O_3-Mo$, where the bonding aligns along the a-axis (figure 1(c)) [41, 43]. The band observed at 667 cm^{-1} can be attributed to the stretching mode of the triply coordinated oxygen (Mo_3-O) resulting from edge sharing [44]. A sheared mode was observed at 375 cm^{-1} and O–Mo–O bending mode was observed at 337 cm^{-1} [45]. Moreover, the wagging modes of the terminal O = Mo = O groups exhibited vibrational modes at 127 cm^{-1}, 284 cm^{-1} and 293 cm^{-1} [41, 43, 45]. The torsional mode involving O = Mo = O is detected at 243 cm^{-1}, while the 157 cm^{-1} peak comes from the translation vibration of the rigid chains [45, 46]. On the other hand, no additional modes resulting from the inclusion of dopant atoms were detected. However, the intensity of the vibrational modes changes with the addition of dopant atoms, suggesting that the addition of dopant atoms primarily leads to defects and oxygen vacancies without causing any structural transformation [42]. The slight broadening/narrowing and shifting of Raman active modes are due to the presence of oxygen vacancies formed by the displacement of oxide ions from their normal cages (figure 1(d)).

The average crystallite sizes (D), dislocation densities and strain values, acquired from XRD patterns using (020) peak, are presented in table 1. The values of *D* were found to be approximately 62.9, 47.3, 46.4, 45.0, 52.6
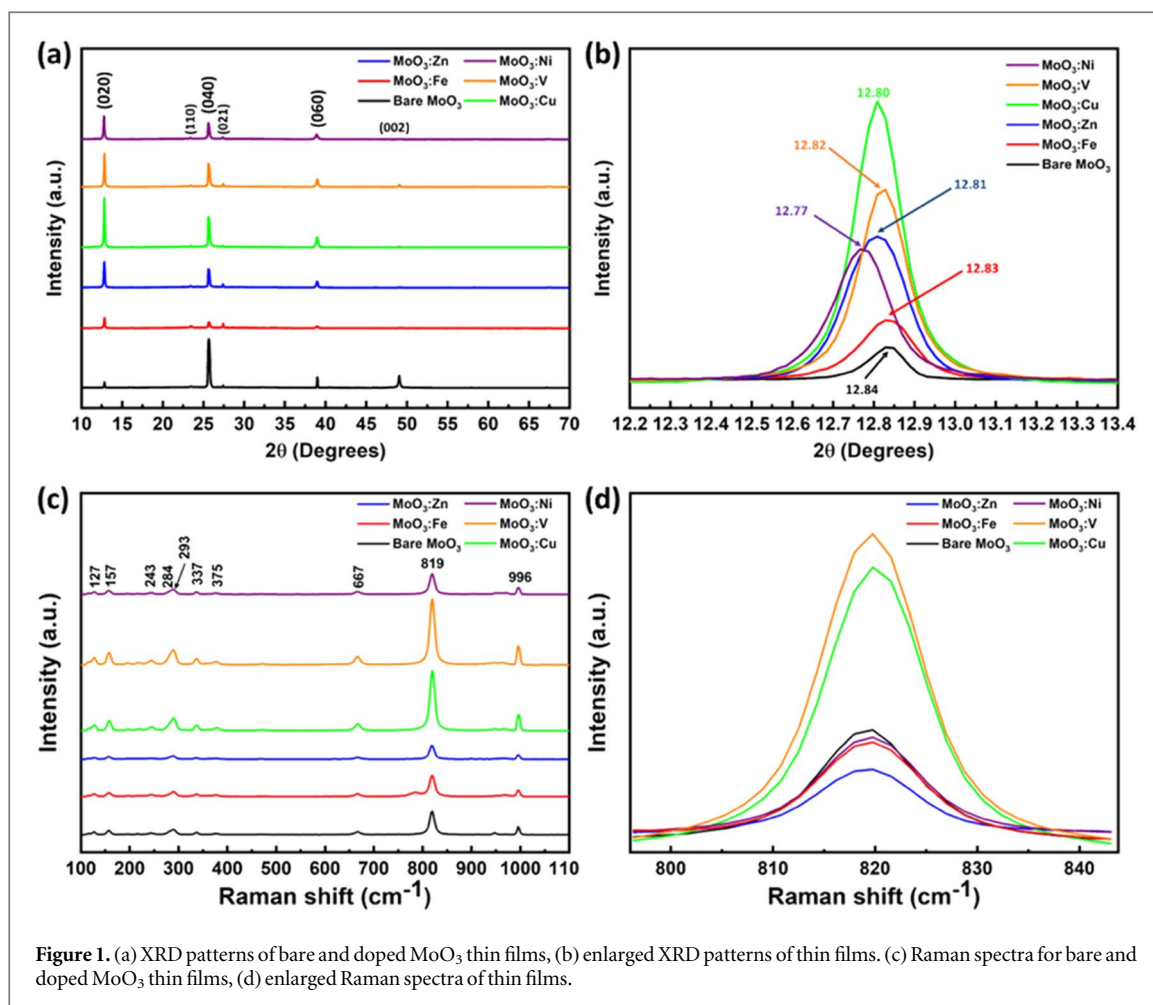
Figure 1. (a) XRD patterns of bare and doped MoO_3 thin films, (b) enlarged XRD patterns of thin films. (c) Raman spectra for bare and doped MoO_3 thin films, (d) enlarged Raman spectra of thin films.

Table 1. Microstructural properties of MoO_3 thin films.

	Diffraction angle (2θ) deg.	hkl	FWHM (degrees)	Dislocation density $\times 10^{-3}$ (nm^{-2})	Crystallite size (D) nm	Micro strain (ε) $(\times 10^{-3})$
MoO_3	12.84	020	0.1318	0.25	62.88	5.14
MoO_3:Fe	12.83	020	0.1764	0.45	47.33	6.85
MoO_3:Zn	12.81	020	0.1799	0.46	46.41	6.99
MoO_3:Cu	12.80	020	0.1854	0.49	45.03	7.21
MoO_3:V	12.82	020	0.1587	0.36	52.60	6.16
MoO_3:Ni	12.77	020	0.1833	0.48	45.56	7.15

and 45.6 nm for bare α-MoO_3, MoO_3:Fe, MoO_3:Zn, MoO_3:Cu, MoO_3:V and MoO_3:Ni films, respectively, which were calculated using the Scherrer's equation ($D = 0.94\lambda/\beta\cos\theta$). Herein, θ is the Bragg angle, β is the FWHM and λ refers to the wavelength of the x-ray. The crystallite size of bare MoO_3 thin film is observed to be larger than doped MoO_3 thin films. Fe, Zn, Cu, V and Ni atoms can act as barriers and inhibit crystallite size growth in doped MoO_3 thin films due to lattice strain. On the other hand, dislocation is a line defect, it increases in decreasing crystallite size and causes an increase in strain. Dislocation densities of doped MoO_3 thin films increase compared to bare MoO_3 thin films due to the presence of dopant atoms. Additionally, as the crystallite size decreases, the defect concentration in doped MoO_3 thin films increases, which increases the dislocation density [8, 47]. The microstrain (ε) values are found to be approximately 5.1, 6.8, 7.0, 7.2, 6.2 and 7.2 $.10^{-3}$ $lin.^{-2}m^{-4}$ for bare MoO_3, MoO_3:Fe, MoO_3:Zn, MoO_3:Cu, MoO_3:V and MoO_3:Ni films respectively, which are calculated using relation $\varepsilon = (\beta\cos\theta)/4$ (table 1).

SEM analysis is carried out for the structural investigation of bare and Fe, Zn, Cu, V and Ni doped α-MoO_3 thin films, which are given in figures 2(a)–(f), respectively. The emergence of different morphologies for bare and doped thin films showed that morphology change can be achieved by doping. Figure 2(a) indicates the layered structure of α-MoO_3 with plate-like structures stacked on top of each other. The layered plate-like
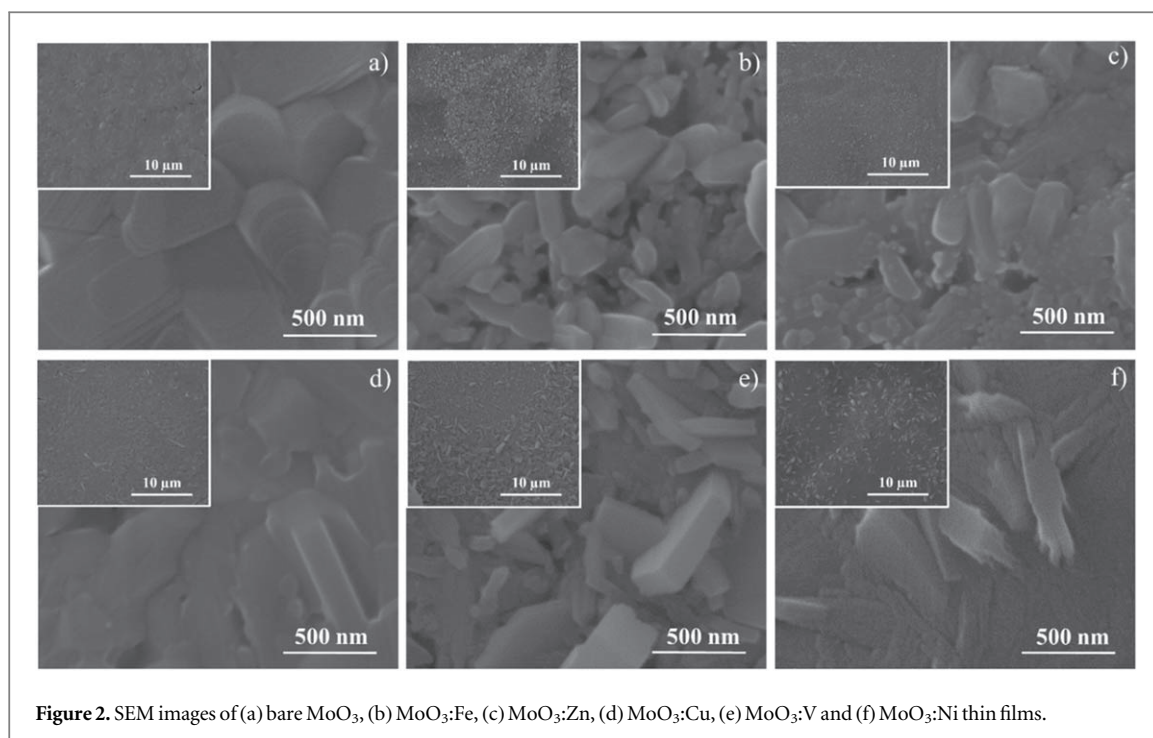
Figure 2. SEM images of (a) bare MoO_3, (b) MoO_3:Fe, (c) MoO_3:Zn, (d) MoO_3:Cu, (e) MoO_3:V and (f) MoO_3:Ni thin films.

Table 2. EDX results of MoO_3 thin films.

Sample	Mo(wt%)	O(wt%)	Fe(wt%)	Zn(wt%)	Cu(wt%)	V(wt%)	Ni(wt%)
MoO_3	84.28	15.72	—	—	—	—	—
MoO_3:Fe	81.59	13.22	5.19	—	—	—	—
MoO_3:Zn	77.96	16.78	—	5.26	—	—	—
MoO_3:Cu	78.70	16.14	—	—	5.16 -	—	
MoO_3:V	78.65 s	15.62	—	—	—	5.73	—
MoO_3:Ni	78.33	16.09	—	—	—		5.58

morphology of bare α-MoO_3 thin film changed to a lamella-like structure upon doping with Fe and Zn. In addition, the lamella-like morphology of MoO_3:Fe consists of some pebble structures, while the amount of the pebble structures increases in MoO_3:Zn thin films, shown in figures 2(b)–(c). On the other hand, MoO_3:Cu thin film has some rod-like structures with irregular shapes (figure 2(d)). The lamellar structure is preserved both for V and Ni doped MoO_3 thin films, except for minor morphological changes figures 2(e)–(f). The lamellar structure had some irregular shapes for the V doped MoO_3 thin film, while agglomeration of the lamellar structure is observed for Ni doped MoO_3 thin film. Furthermore, the lamella-like structure observed in SEM images are consistent with (0k0) planes seen in the XRD pattern in figure 1(a). Also, EDX is conducted for further analysis and obtained results are given in table 2 proved that the concentration of dopants is around 5 wt%.

3.2. Linear optical analysis

Figure 3(a) shows the linear absorption spectra of the MoO_3 thin films. Doping is found to increase the absorption and slightly shift the band edge to longer wavelengths with decreased steepness. This observation showed that doped thin films contain increased number of defect states, in particular point defects. To clarify the NA mechanisms, it is necessary to determine the bandgap energy of the materials. The bandgap energy is obtained by the Tauc plot using the below expression [49].

$$\alpha h\nu \;=\; A(h\nu - E_g)^n \tag{1}$$

where $n = 1/2$ and $n = 2$ for direct and indirect transitions taking place between valence and conduction bands, respectively. E_g is the bandgap energy, A is a constant, $h\nu$ is the photon energy and α is the linear absorption coefficient. Figure 3(b) demonstrates the Tauc plots ($(\alpha h\nu)^2$ versus $h\nu$ graphs) and obtained bandgap values are tabulated in table 3. Bandgap of the bare MoO_3 reduced from 3.85 eV to 3.34 eV with dopants. These dopant atoms created localized defect states just below the conduction band. These defect states caused to
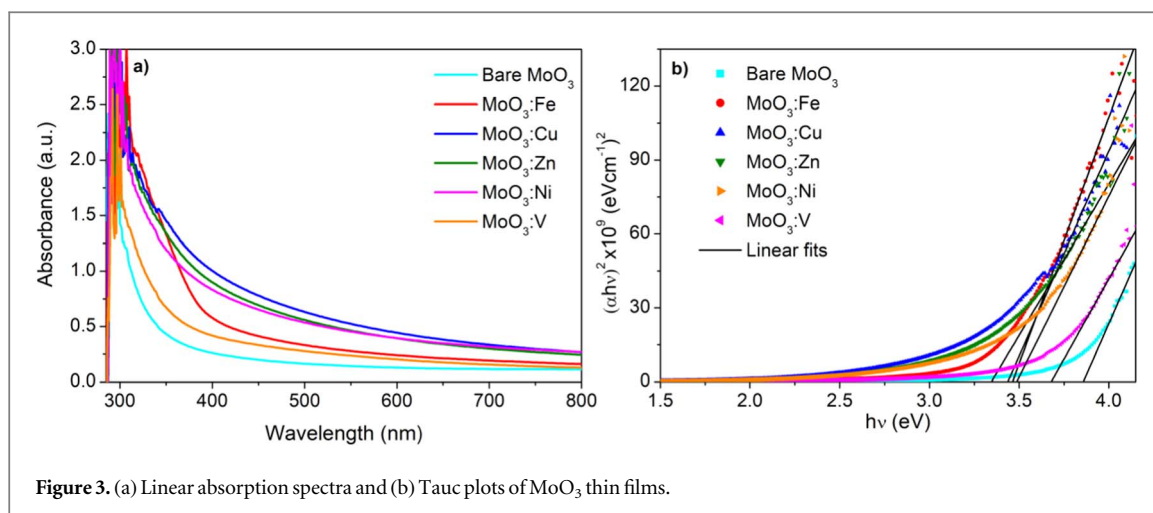
Figure 3. (a) Linear absorption spectra and (b) Tauc plots of MoO$_3$ thin films.

Table 3. Bandgaps (E_g) and urbach energy values (E_U) of the MoO$_3$ thin films.

Samples	E_g (eV)	E_U (eV)
MoO$_3$	3.85	0.54
MoO$_3$:Fe	3.46	0.59
MoO$_3$:Cu	3.43	1.36
MoO$_3$:Zn	3.34	1.18
MoO$_3$:Ni	3.48	1.24
MoO$_3$:V	3.67	0.81

reduced band gap energy. The obtained E_g value of the bare α-MoO$_3$ was consistent with the literature values [50, 51].

Urbach energy of the materials supplies information on the defect states density within the bandgap. The Urbach energies are investigated to reveal the effect of dopant atoms on the defect states density of the MoO$_3$ thin films. The Urbach formula [52] expressed as below is used to find out the Urbach energy.

$$\alpha = \alpha_0 \exp\ (h\nu/E_U) \tag{2}$$

where α_0 is a constant, E_U is the Urbach energy and α is the absorption coefficient. The inverse slope of the linear region of the $ln\alpha$ versus $h\nu$ graphs shown in figure 4 provides the Urbach energies and increased E_U is observed with doping. Considering the obtained linear optical results, it can be stated that the dopant atoms cause an increase in the defect states of the MoO$_3$ thin films, as indicated by XRD results.

3.3. Photoluminescence and femtosecond transient absorption spectroscopy analysis

Figure 5 indicates the photoluminescence spectra of the MoO$_3$ thin films excited by a wavelength of 320 nm at room temperature. The broad photoluminescence signals are observed between 350 and 600 nm, as also reported in the literature [53]. Photons with energies over their bandgaps reflected off the samples and produced unstable photo-excited electrons. This caused them to return to a ground state and release less energetic fluorescence photons. The strong fluorescence emission at 379 nm is shown due to electron–hole recombination and, its intensity decreased and shifted to the longer wavelengths with doping. In the present research, the weak emission signals, which are caused by the electron–hole recombination between the conduction band and the sublevel of adsorbed oxygen acceptors (defect states in the energy band gap) [54], are also detected at 486 and 531 nm, and these are found to increase with dopant atoms (Fe, V, Ni, Zn, Cu). The observed increasing intensity of these signals in doped MoO$_3$ thin films signed out the increased defect states in the energy region of the 486 and 531 nm.

Defect assisted excited state absorption (ESA) is only observed when the lifetime of the localized defect states are longer than the laser pulse duration. Figure 6 indicates the time evolution of the pump–probe data of MoO$_3$ thin films. The normalized transmission is found to decay with three exponential times. Continuous ESA is observed with the ultrafast pump–probe experiments. The fastest time component (about 0.5–1 ps) is attributed to the hot carrier gas interaction with the lattice and cooling down to lattice temperature in MoO$_3$ thin films. The second time component which is around 70–100 ps could be the recombination processes without getting

Figure 4. $\ln\alpha$ versus $h\nu$ plots of MoO_3 thin films.

Figure 5. Photoluminescence spectra of MoO_3 thin films.
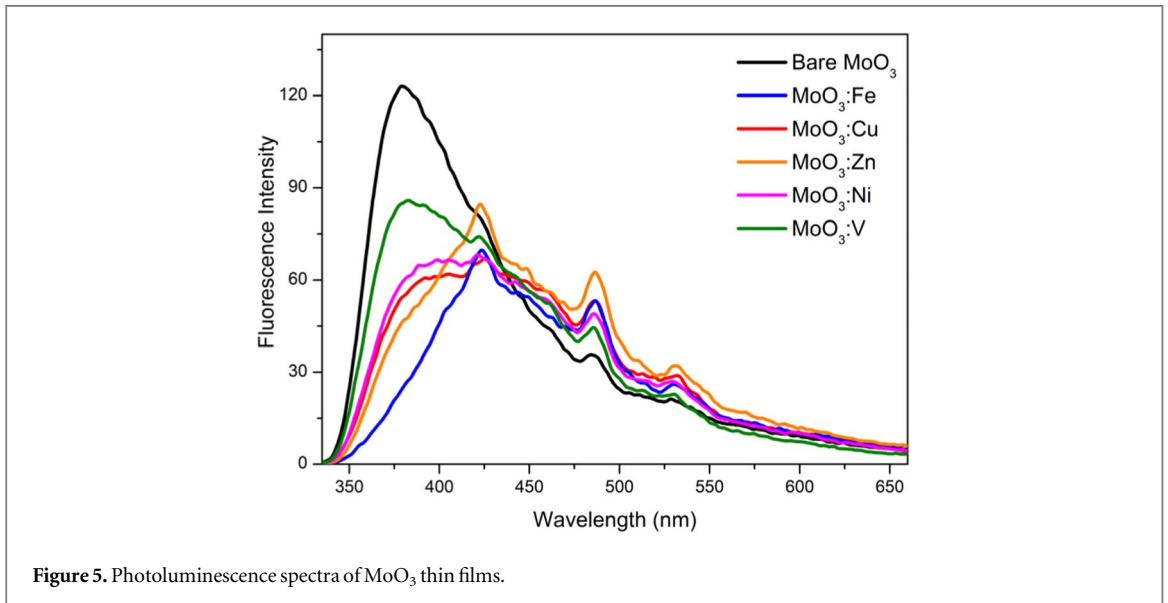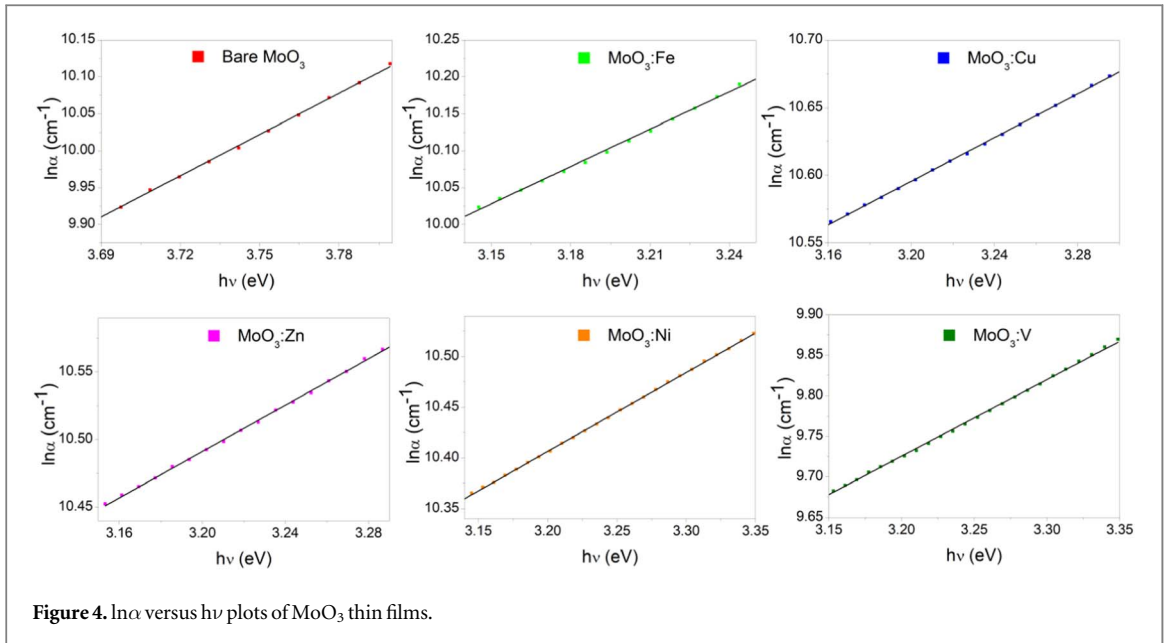
trapped by the defect states. The slowest component ($\gg 4$ ns) is attributed to the carrier vanishing either by getting trapped by localized defect states or recombined at recombination centers after cooling. Based on the results, it can be said that these defect states can be saturated and this will be explained in the next section.

3.4. Nonlinear absorption and optical limiting analysis

Open aperture (OA) Z-scan experiments at an excitation wavelength of 532 nm under various input intensities are performed to reveal the NA features of bare and Fe, V, Ni, Zn and Cu doped MoO_3 thin films. In model 1, the OA Z-scan curves were fitted to 2PA procedure introduced by Sheik-Bahae *et al* [55]. The two photon absorption coefficient was found from fitting of OA Z-scan data into equation (3).

$$T(z) = \sum_{m=0}^{\infty} \frac{q_0}{(m+1)^{3/2}(1+z^2/z_0^2)^m} \tag{3}$$

where m is an integer, q_0 (z) is $\beta I_0 L_{eff}$, β is the 2PA coefficient and the effective thickness is $L_{eff} = \frac{1-e^{-\alpha_0 L}}{\alpha_0}$ with the sample thickness L, and α_o is the linear absorption coefficient. Figure 7 indicates the OA Z-scan curves of the thin films at 40.04 MW cm^{-2} input intensity. Their 2PA coefficients were found as 5.67×10^{-8}, 8.93×10^{-8}, 1.32×10^{-7}, 1.77×10^{-7}, 3.31×10^{-6} and 5.11×10^{-6} m/W for bare MoO_3, and Ni, Fe, V, Zn and Cu
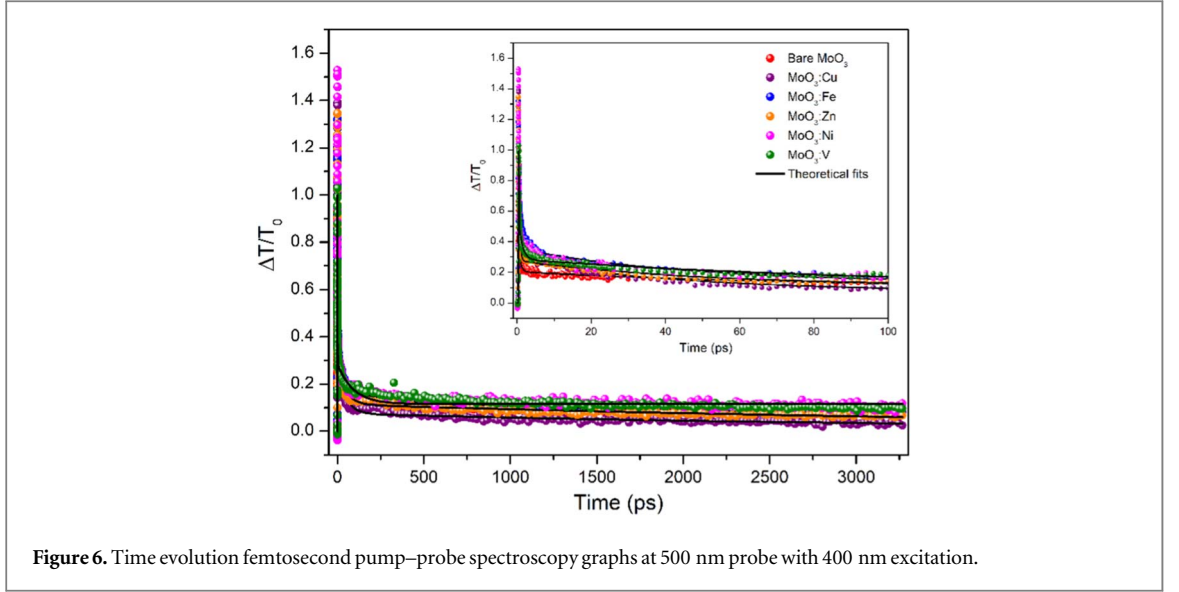
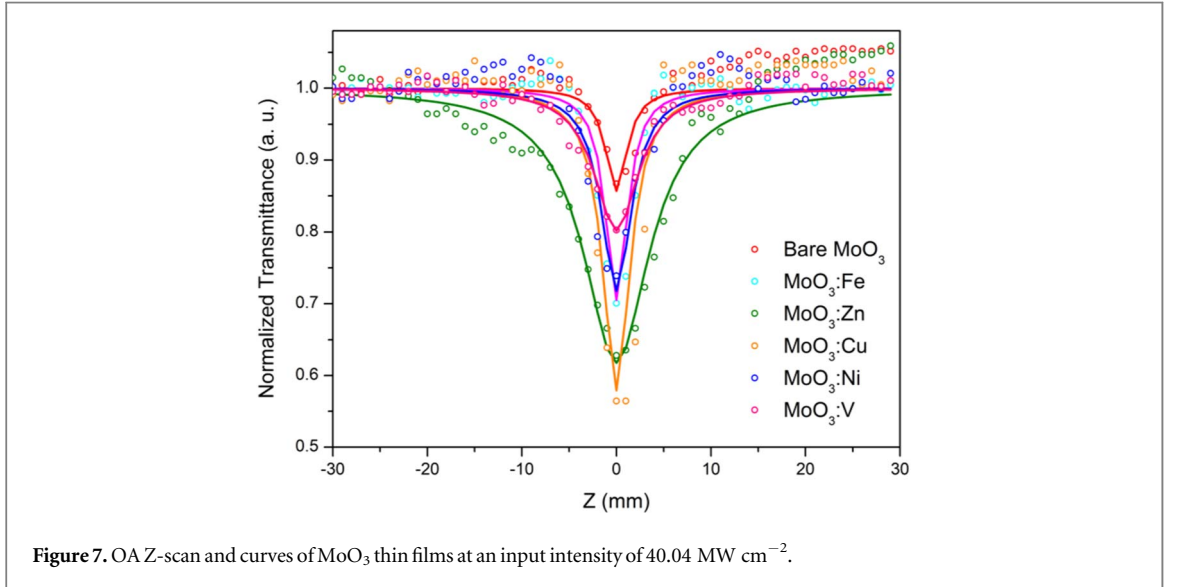**Figure 6.** Time evolution femtosecond pump–probe spectroscopy graphs at 500 nm probe with 400 nm excitation.

Figure 7. OA Z-scan and curves of MoO$_3$ thin films at an input intensity of 40.04 MW cm^{-2}.

doped MoO$_3$ thin films respectively. It revealed that the doping atoms led to stronger NA behavior as compared to bare MoO$_3$ thin films.

Moreover, all of the MoO$_3$ thin films have the defective structure as presented in the previous section and these defect states contribute to NA behaviors of the materials. Therefore, in model 2, Z-scan data are fitted using a theoretical model that takes into account the contribution of one photon absorption (OPA), 2PA and free carrier absorption (FCA) to NA.

$$\frac{dI}{dz} = \frac{\alpha I}{1 + I/I_{SAT}} - \frac{\beta I^2}{1 + I^2/I_{SAT}^2} - \frac{\sigma_0 \Delta N(I) I}{1 + I^2/I_{SAT}^2} \tag{4}$$

In this model, the first term represents the OPA and its saturation, the second term represents 2PA and its saturation, and the last term represents FCA and its saturation. In equation (4), $\Delta N(I)$ is the generated photo carrier density given as

$$\Delta N = \frac{\alpha I}{\hbar \omega} \tau_0 + \frac{\beta I^2}{2 \hbar \omega} \tau_0 \tag{5}$$

where α is the linear absorption coefficient, $\hbar \omega$ is the photon energy, β is the 2PA coefficient and τ_0 is the pulse duration. Substituting equation (5) in equation (4), the expression can be obtained as below. According to our model, the optical intensity (I) loss while propagating in the sample is governed by the differential equation.
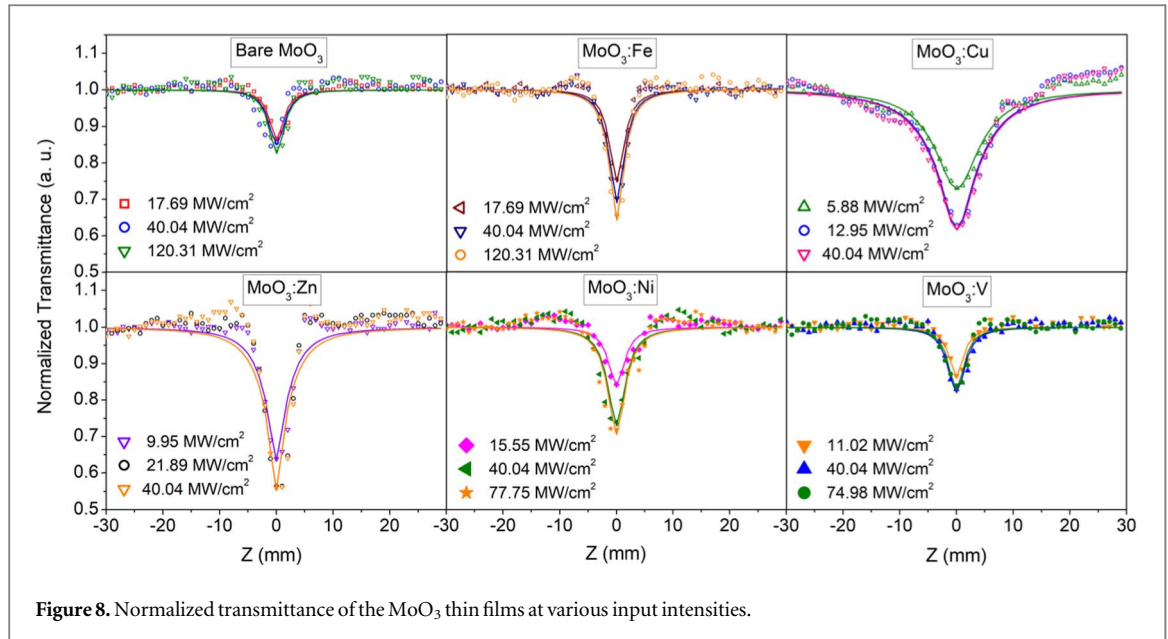
Figure 8. Normalized transmittance of the MoO$_3$ thin films at various input intensities.

$$\frac{dI}{dz'} = \frac{\alpha I}{1 + I/I_{SAT}} - \frac{\beta_{eff} I^2}{1 + I^2/I_{SAT}^2} \tag{6}$$

In equation (6), z' is the propagation distance inside the sample, I_{SAT} is the saturation intensity threshold and β_{eff} is the effective NA coefficient given in the following

$$\beta_{eff} = \beta + (\sigma_0 \alpha \tau_0 / \hbar \omega) \tag{7}$$

where σ_0 is the FCA cross section. The fitting details are given in [56]. The laser pulse energy was fixed at 0.5, 1.1 and 3.4 μJ for all of the prepared thin films in Z-scan experiments. The ω_o value was obtained from the fitting of the experimental data and it was found in the range of 15 μm and 26 μm for bare and doped MoO$_3$ thin films. Nonlinear optical features of the MoO$_3$ thin films at various input intensities are presented in figure 8. All of the thin films showed NA behavior and the normalized transmittance reduced with an increase of the input intensity. The OA Z-scan curve width increased with the dopant atoms (Fe, Zn, Cu, Ni and V) as can be seen in this figure.

In our model, we considered OPA, 2PA and FCA contributions due to defect states within the energy bandgap. The type of 2PA can be distinguished by the inclusion of intermediate states, (i) Genuine 2PA is the simultaneously two photon absorptions through the virtual state, and (ii) sequential 2PA or OPA + ESA is sequential absorption of photons [57]. In contrast to genuine 2PA, ESA occurs when the electron in excited state absorbs one more excitation photon before it decays to the ground state. Z-scan cannot determine the nature of 2PA, so intensity dependent NA measurement must be carried out to determine the true mechanism underlying 2PA. When the NA coefficient is independent of the input intensity, genuine 2PA is prevalent. When the NA coefficient changes (increases/decreases) with increasing of input intensity, ESA process will become dominant. This is due to excitation of electron from the ground state to excited state, which depletes the ground state population [58]. To identify the involved 2PA process, intensity dependent NA studies are conducted. Figure 9 shows the variation of β_{eff} with respect to input intensities. It is clear that the NA coefficient remained constant with varying input intensity and yielded genuine 2PA for bare, Fe- and V-doped MoO$_3$ thin films, while for Zn, Cu and Ni-doped thin films, the NA coefficient changed with varying input intensity assuring the occurrence of sequential 2PA. As can be seen in this figure, β_{eff} decreased rapidly for Zn and Cu doped MoO$_3$ thin films with higher defect states among other doped thin films. NA behaviors are strongly influenced by the filling of these defect states, which caused saturable absorption. On the other hand, other thin ffilms with low defect states can be saturated at low input intensity, so β_{eff} values slightly change or remained unchanged with increasing input density. In the case of sufficient laser light intensity, the pure saturable absorption can be observed in our experiments. Although the OPA induced saturable absorption effect led to decrease the NA, the pure saturable absorption curves were not observed due to insufficient laser light intensity.

The normalized transmittances of thin films at 40.04 MW cm^{-2} are presented in figure 10(a). It is clearly seen that NA was strengthened by the influence of the contributing atoms. The increasing width is an indication that the contribution of OPA to NA is increasing. The OA Z-scan curves width increased with doping atoms, and wider width was observed for MoO$_3$:Cu thin film among other thin films. This means that the contribution of OPA to NA is higher for Cu doping. Theoretical fitting results of the data are presented in table 4. β_{eff} increased
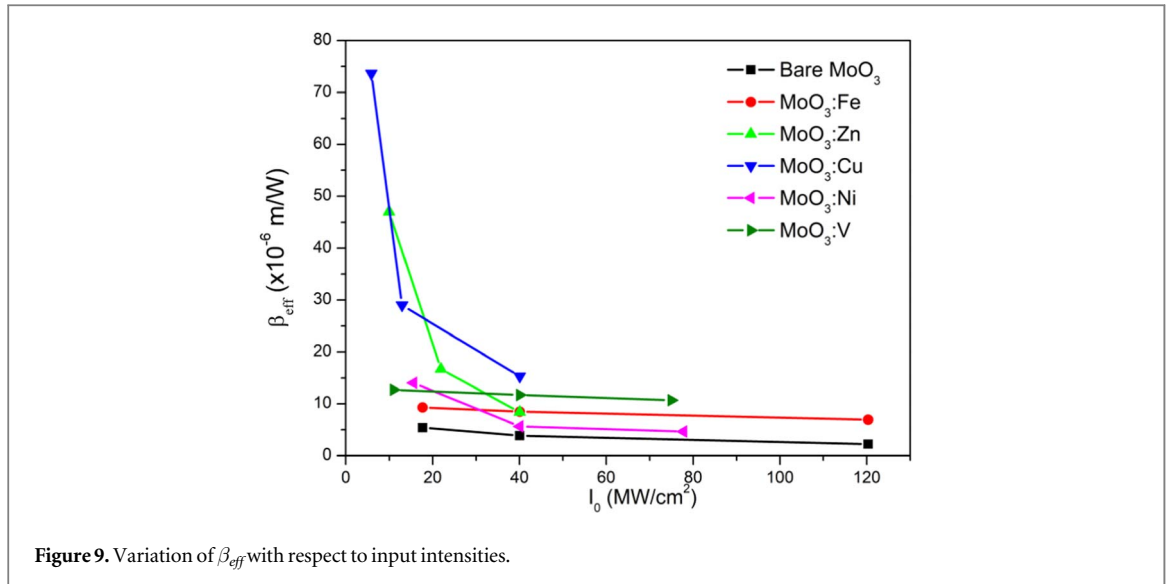
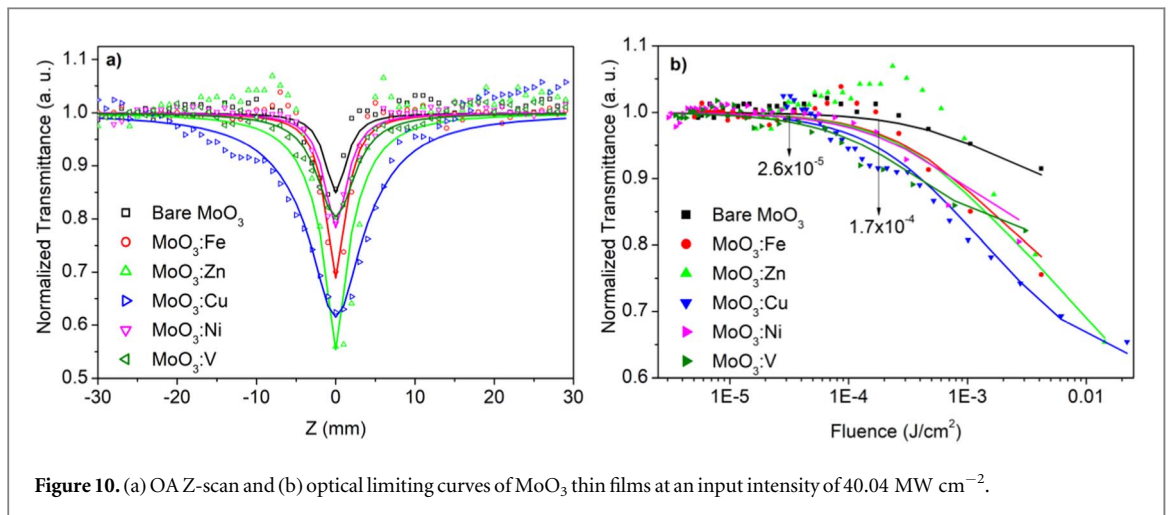**Figure 9.** Variation of β_{eff} with respect to input intensities.

Figure 10. (a) OA Z-scan and (b) optical limiting curves of MoO$_3$ thin films at an input intensity of 40.04 MW cm^{-2}.

Table 4. Nonlinear absorption coefficients (β_{eff}), saturation intensity threshold (I_{SAT}) and optical limiting threshold values of the MoO$_3$ thin films under a 532 nm laser excitation at an input intensity of 40.04 MW cm^{-2}.

Exc. wavelength	β_{eff} (m/W)	I_{SAT} (W/m^2)	Onset Opt. lim. thres. (mJ/cm^2)
MoO$_3$	3.87×10^{-6}	7.16×10^{11}	0.170
MoO$_3$:Fe	8.48×10^{-6}	1.25×10^{12}	0.065
MoO$_3$:Zn	1.67×10^{-5}	7.68×10^{13}	0.031
MoO$_3$:Cu	2.90×10^{-5}	7.89×10^{13}	0.026
MoO$_3$:V	1.28×10^{-5}	1.47×10^{12}	0.040
MoO$_3$:Ni	1.40×10^{-5}	2.40×10^{12}	0.034

from 3.87×10^{-6} to 2.90×10^{-5} m W^{-1} with doping atoms. Among the dopant atoms, the bigger β_{eff} is obtained for Cu dopant. Considering the bandgap energy (3.85 eV) of bare α-MoO$_3$ thin film, an electron can be excited from the valence band to the conduction band by genuine 2PA with an energy of 2.32 eV. In this case, the dominant NA mechanism is 2PA. Although MoO$_3$:Fe and MoO$_3$:V thin films have higher number defect states with respect to bare thin film, used light energy is not sufficient to excite an electron from valence band to defect states. Therefore, these thin films had the same NA mechanism as the bare thin film. On the other hand, as discussed in the previous section, the E_u energy increased to 1.18, 1.24 and 1.36 eV for Zn, Ni and Cu doping atoms, respectively. Therefore, the electron can be excited from the valence band to the defect states in the bandgap with OPA (2.32 eV) and then excited from defect states to conduction band by absorption of another photon. Therefore, the dominant NA mechanisms for the Zn, Ni and Cu doped MoO$_3$ thin films are OPA and

Figure 11. Proposed possible NA mechanisms for bare MoO$_3$ and Cu doped MoO$_3$ thin films.
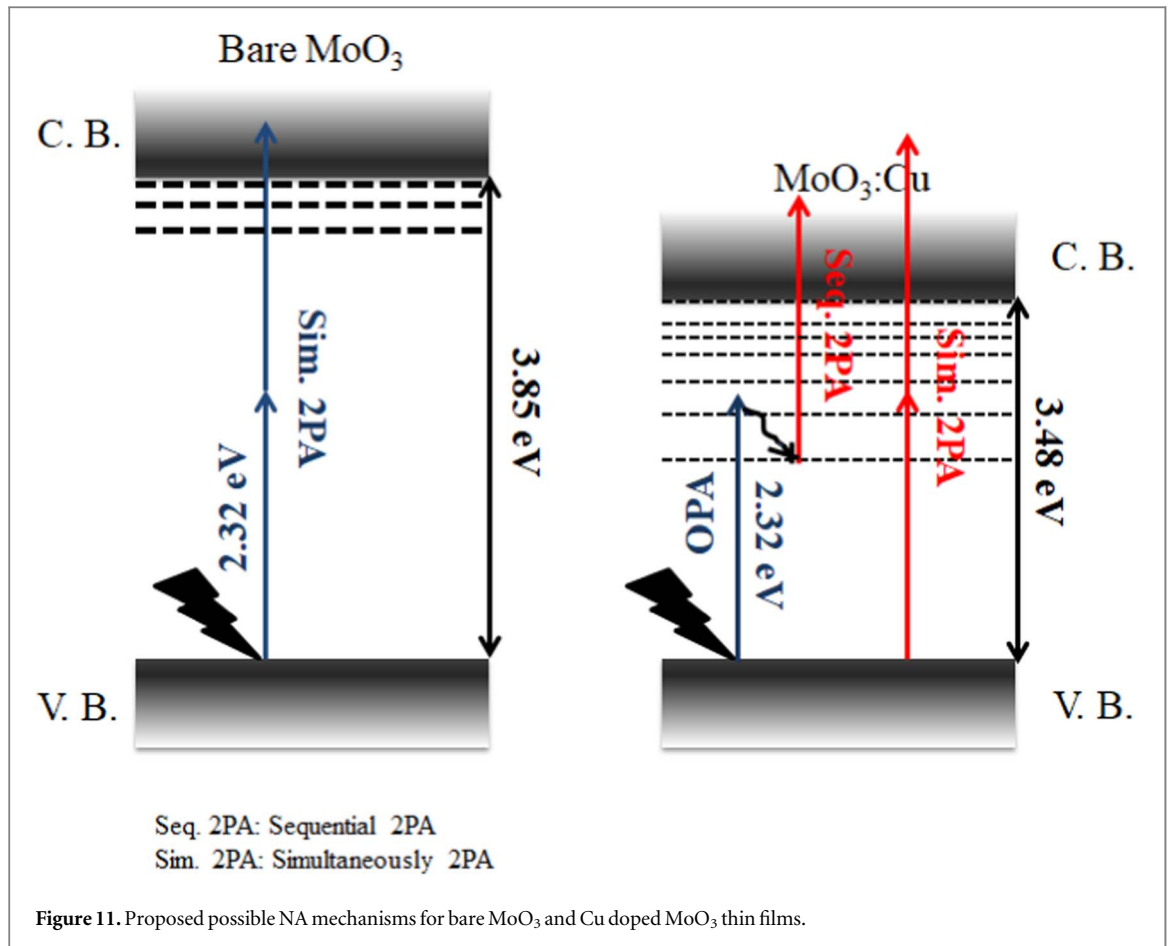
2PA (simultaneously 2PA and sequential 2PA). The results revealed that increasing density of defect states increases the NA behavior of MoO$_3$ thin films. As compared the NA coefficient values, NA coefficient values in model 2 are 100 times higher than the values in model 1. Due to the defect states assisted NA mechanisms caused to higher NA coefficient. The effect of defect states on NA was reported in the literature [10, 22, 24, 28, 59, 60]. The I_{SAT} value increased from 7.16×10^{11} W m^{-2} to 7.89×10^{13} W m^{-2} with doping atoms compared to the bare α-MoO$_3$ thin film owing to the increased defect states density inside the bandgap with dopant atoms. The obtained β_{eff} values of doped MoO$_3$ thin films are higher than the values of [42, 61].The [42] reported that β values changed with different morphology of the MoO$_3$ (Nano-Rods, -Wires, -Belts and –Tubes). They reported that the defects in different morphology created by ZnO. The [61] reported that β_{eff} values increased with increase of the GO concentration in MoO$_3$. It was observed in the present study that the doping atom in MoO$_3$ increased the defect states in the structure and changed the morphology of the bare MoO$_3$. The NA coefficient of the bare MoO$_3$ thin film increased due to the increasing defect states and changing morphology. On the other hand, NA is affected by many parameters such as the production method, doping sample, temperature, morphology, density and distribution of defect states. Considering all of these, no single parameter can be put forward as the reason for the obtained results. Possible NA mechanisms for MoO$_3$ thin films are presented in figure 11.

The negative impact of high-power laser technology on society is the potential for unintentional exposure to powerful laser pulses, causing irreparable damage to human eyes, skin, and optical detectors. Researchers have been motivated by this to investigate and design innovative materials with strong and high linear transmittance, broad-band passive optical limiting, quick reaction times, and high thresholds for laser damage [61]. An ideal optical limiter limits the transmitted light over its optical limiting thresholds and holds it constant, and in this way it protects the sensitive devices. It is known that the optical limiting response will be higher if the optical limiting threshold is lower. The optical limiting curves of the thin films are presented in figure 10(b) and the values are listed in table 4. Optical limiting threshold of the bare α-MoO$_3$ thin film decreased with doping from 0.17 to 0.065, 0.040, 0.034, 0.031 and 0.026 mJ/cm^2 for Fe, V, Ni, Zn and Cu doping, respectively. The MoO$_3$:Cu thin film indicated higher optical limiting feature owing to the its stronger NA behavior among other thin films. Our results indicate that the MoO$_3$:Cu thin film can be a good candidate as an effective optical limiter in the visible wavelength region. The films of present materials can be used as an external optical component which is

directly interacted with the high power light before sensitive component or protection can be provided by coating the optically sensitive element with these materials that have optical limiting properties.

4. Conclusions

In this work, bare and Fe, Zn, V, Ni and Cu doped MoO_3 thin films were deposited onto pre-heated glass substrates using USD method. The XRD results showed that all the diffraction peaks of the thin films could be indexed to the orthorhombic structure of α-MoO_3 without any extra peaks related to other elements or intermetallics. Upon doping, the changes in the morphology, linear and NA features of MoO_3 thin films were observed. Linear optical analysis showed that the bandgap of the bare thin film decreased and the Urbach energy increased owing to an increase in the defect states upon doping. The broad strong fluorescence emission was observed in the range of 350 and 600 nm with a decreasing intensity upon doping. The weak photoluminescence signals were detected at 486 and 531 nm and the photoluminescence intensity was found to increase upon doping. The OA Z-scan measurement results revealed the NA behavior of the bare and Fe, Zn, V, Ni and Cu doped MoO_3 thin films. NA behavior of all the thin films became stronger with increasing input intensity and doping. The 2PA coefficient value of the bare thin film increased with doping atoms and they were found in the range of 5.67×10^{-8} and 5.11×10^{-6} m W^{-1}. The NA coefficient value of bare thin film increased from 3.87×10^{-6} m W^{-1} to 8.48×10^{-6}, 1.28×10^{-5}, 1.40×10^{-5}, 1.67×10^{-5}, 2.90×10^{-5} with Fe, V, Ni, Zn and Cu dopants, respectively. The NA coefficient values are 100 times higher than that of 2PA coefficient values due to the strong contribution of defects to NA. The NA mechanisms of the MoO_3 thin films were also elucidated. Considering their linear optical results, genuine 2PA was the dominant NA mechanism for the bare, Fe and V doped MoO_3 thin films. OPA was enough to excite an electron from valance band to defect states due to higher defect states density of the Ni, Zn and Cu doped thin films. Therefore, the NA mechanisms were OPA and 2PA (two steps sequential ESA) for these thin films. The OA Z-scan results revealed the strong influence of the defects on the NA behavior of the MoO_3 thin films. Investigation of the optical limiting behavior demonstrated that the Cu doped MoO_3 thin film had lower optical limiting threshold as 0.026 mJ/cm^2 among the other dopants in line with the NA results. Considering all the results together, Ni, Zn and Cu doped MoO_3 thin films are highly promising candidates as optical limiters in the visible wavelength region, due to their higher NA behavior and lower optical limiting thresholds.

Data availability statement

The data cannot be made publicly available upon publication because they are not available in a format that is sufficiently accessible or reusable by other researchers. The data that support the findings of this study are available upon reasonable request from the authors.

Declaration of interests

There are no conflicts to declare.

ORCID iDs

Yasemin Pepe https://orcid.org/0000-0002-5384-2039
Husnu Emrah Unalan https://orcid.org/0000-0003-3667-179X

References

[1] Hsu C S, Chan C C, Huang H T, Peng C H and Hsu W C 2008 *Thin Solid Films* **516** 4839–44
[2] Dhanasankar M, Purushothaman K K and Muralidharan G 2010 *Mater. Res. Bull.* **45** 1969–72
[3] Chandoul F, Boukhachem A, Hosni F, Moussa H, Fayache M S, Amlouk M and Schneider R 2018 *Ceram. Int.* **44** 12483–90
[4] Mahajan S S, Mujawar S H, Shinde P S, Inamdar A I and Patil P S 2009 *Sol. Energ Mat. Sol. C* **93** 183–7
[5] Ijeh R O, Nwanya A C, Nkele A C, Madiba I G, Bashir A K H, Ekwealor A B C, Osuji R U, Maaza M and Ezema F 2020 *Ceram. Int.* **46** 10820–8
[6] Liu S H, Zhang X, Wang S R, Feng H W, Zhang J X, Yang H S, Zhang L T and Xie W F 2018 *Org. Electron.* **52** 264–71
[7] Morales-Luna M, Arvizu M A, Perez-Gonzalez M and Tomas S A 2019 *J. Phys. Chem. C* **123** 17083–91
[8] Tutel Y, Koylan S, Tunca S and Unalan H E 2021 *ACS Appl. Nano Mater.* **4** 13871–83
[9] Tutel Y *et al* 2021 *J. Electrochem. Soc.* **168** 106511
[10] Pepe Y, Tutel Y, Yildiz E A, Karatay A, Unalan H E and Elmali A 2021 *Adv. Eng. Mater.* **23** 2100468
[11] Li C P, Wolden C A, Dillon A C and Tenent R C 2012 *Sol. Energ Mat. Sol. C* **99** 50–5

[12] Oluwabi A T, Katerski A, Carlos E, Branquinho R, Mere A, Krunks M, Fortunato E, Pereira L and Acik I O 2020 *J. Mater. Chem. C* **8** 3730–9

[13] Zeggar M L, Chabane L, Aida M S, Attaf N and Zebbar N 2015 *Mat. Sci. Semicon Proc* **30** 645–50

[14] Chen Z J, Dedova T, Spalatu N, Maticiuc N, Rusu M, Katerski A, Acik I O, Unold T and Krunks M 2022 *Colloid Surface*A **648** 129366

[15] Tutel Y, Durukan M B, Hacioglu S O, Baskose U C, Toppare L and Unalan H E 2023 *Applied Materials Today* **35** 101924

[16] Lin J M *et al* 2020 *Nanoscale* **12** 23140–9

[17] Sen S K, Dutta S, Paik L, Paul T C, Manir M S, Hossain M and Hossain M N 2021 *J Alloy Compd* **876** 102404

[18] Sen S K, Jalil M, Hossain M, Manir M, Hoque K, Islam M and Hossain M 2021 *Materials Today Communications* **27** 102404

[19] Boukhachem A, Mokhtari M, Benameur N, Ziouche A, Martínez M, Petkova P, Ghamnia M, Cobo A, Zergoug M and Amlouk M 2017 *Sens. Actuators, A* **253** 198–209

[20] Sutherland R L 2003 *Handbook of nonlinear optics* (CRC press)

[21] Thomas P, Sreekanth P, Philip R and Abraham K E 2015 *RSC Adv.* **5** 35017–25

[22] Pepe Y, Akkoyun S, Karatay A, Yildiz E A, Unver H, Ates A and Elmali A 2022 *J. Appl. Polym. Sci.* **139** 1058–68

[23] Pepe Y, Akkoyun S, Karatay A, Yildiz E A, Ates A, Unver H and Elmali A 2022 *J. Mater. Sci.* **57** 1058–68

[24] Unlu B A, Karatay A, Yildiz E A, Dincbay T, Unver H, Gasanly N and Elmali A 2022 *J. Lumin.* **241** 106230

[25] Ünlü B A, Karatay A, Yüksek M, Ünver H, Gasanly N and Elmali A 2020 *Opt. Laser Technol.* **128** 106230

[26] Unlu B A, Karatay A, Avci E, Yildiz E A, Ates A and Elmali A 2022 *J. Lumin.* **248** 118987

[27] Unlu B A, Sener D, Tekin S, Yildiz E A, Karatay A, Serin T and Elmali A 2021 *Phys. Status Solidi*B **258** 2000539

[28] Lin J, Chen H, Ma D, Gong Y, Li Z, Li D, Song Y, Zhang F, Li J and Wang H 2020 *Nanoscale* **12** 23140–9

[29] Sen S K, Barman U C, Manir M, Mondal P, Dutta S, Paul M, Chowdhury M and Hakim M 2020 *Adv. Nat. Sci.: Nanosci. Nanotechnol.* **11** 025004

[30] Camacho R A P, Tian R X, Liu J, Zhou S Y, Wu A M and Huang H 2021 *Electrochim. Acta* **394**

[31] Ouyang Q-Y, Li L, Wang Q-S, Zhang Y, Wang T-S, Meng F-N, Chen Y-J and Gao P 2012 *Sensors Actuators B* **169** 17–25

[32] Han C, Duan L B, Zhao X R, Hu Z M, Niu Y F and Geng W C 2019 *J. Alloy Compd.* **770** 854–63

[33] Breviglieri S T, Cavalheiro E T G and Chierice G O 2000 *Thermochim. Acta* **356** 79–84

[34] Sen S K, Paul T C, Manir M S, Dutta S, Hossain M N and Podder J 2019 *J Mater Sci-Mater El* **30** 14355–67

[35] Al-Otaibi A L, Ghrib T, Alqahtani M, Alharbi M A, Hamdi R and Massoudi I 2019 *Chem. Phys.* **525**

[36] Kamoun O, Boukhachem A, Amlouk M and Ammar S 2016 *J. Alloy Compd* **687** 595–603

[37] Pandeeswari R and Jeyaprakash B 2014 *Biosens. Bioelectron.* **53** 182–6

[38] Ye M, Sun Q, Chen X Q, Jiang Z H and Wang F P 2012 *J Alloy Compd* **541** 99–103

[39] Boukhachem A, Kamoun O, Mrabet C, Mannai C, Zouaghi N, Yumak A, Boubaker K and Amlouk M 2015 *Mater. Res. Bull.* **72** 252–63

[40] Yan B, Zheng Z, Zhang J, Gong H, Shen Z, Huang W and Yu T 2009 *J. Phys. Chem. C* **113** 20259–63

[41] Illyaskutty N, Sreedhar S, Kohler H, Philip R, Rajan V and Pillai V M 2013 *J. Phys. Chem. C* **117** 7818–29

[42] Guan X, Ren Y, Chen S, Yan J, Wang G, Zhao H, Zhao W, Zhang Z, Deng Z and Zhang Y 2020 *J. Mater. Sci.* **55** 5808–22

[43] Dayal S and Kumar C S 2016 *Mater. Res. Express* **3** 106405

[44] Farzi-kahkesh S, Rahmani M B and Fattah A 2020 *Mater. Sci. Semicond. Process.* **120** 105263

[45] Lv X, Wang S, Gong L, Chen Q, Zhang Y, Chen J and Xie W 2021 *Chem. Phys. Lett.* **779** 138840

[46] Yücel E and Yücel Y 2017 *Ceram. Int.* **43** 407–13

[47] Tutel Y, Koylan S, Tunca S and Unalan H E 2021 *ACS Appl. Nano Mater.* **4** 13871–83

[48] Pankove J I 1971 *optical processes in semiconductors* (Englewood Cliff: New Jersey: Prentice-Hall Inc.) 34–86

[49] Kamoun O, Gassoumi A, Shkir M, Gorji N E and Turki-Kamoun N 2022 *Coatings* **12** 823

[50] Al-Muntaser A A, Nasher M A and Makhlouf M M 2022 *Ceram. Int.* **48** 8069–80

[51] Urbach F 1953 *Phys. Rev.* **92** 1324

[52] Song J, Ni X, Zhang D and Zheng H 2006 *Solid State Sci.* **8** 1164–7

[53] Klinbumrung A, Thongtem T and Thongtem S 2012 *J. Nanomater.* **2012** 930763

[54] Sheik-Bahae M, Said A A, Wei T-H, Hagan D J and Van Stryland E W 1990 *IEEE J. Quantum Electron.* **26** 760–9

[55] Yüksek M, Kürüm U, Yaglioglu H G, Elmali A and Ateş A 2010 *J. Appl. Phys.* **107** 033115

[56] Zheng X Q, Feng M and Zhan H B 2013 *J. Mater. Chem.* **1** 6759–66

[57] Anand B, Krishnan S R, Podila R, Sai S S S, Rao A M and Philip R 2014 *Phys. Chem. Chem. Phys.* **16** 8168–77

[58] Tekin S, Tutel Y, Karatay A, Unalan H E and Elmali A 2022 *J. Lumin.* **252** 119362

[59] Pepe Y, Akkoyun S, Bozkurt B, Karatay A, Ates A and Elmali A 2023 *J. Mater. Chem. C* **11** 2756–63

[60] Ramar V and Karthikeyan B 2020 *Appl. Phys.*A **126** 1–9

[61] Girisun T C S, Saravanan M and Soma V R 2018 *ACS Appl. Nano Mater.* **1** 6337–48